Yin-Yang spiraling transition of a confined buckled elastic sheet

Stéphanie Deboeuf, Suzie Protière, Eytan Katzav

Yin-Yang spiraling transition of a confined buckled elastic sheet

Stéphanie Deboeuf[1],* Suzie Protière[1], and Eytan Katzav[2]
[1] *Sorbonne Université, CNRS, UMR 7190, Institut Jean Le Rond d'Alembert, F-75005 Paris, France and*
[2] *Racah Institute of Physics, The Hebrew University, Jerusalem 9190401, Israel*
(Dated: August 16, 2023)

DNA in viral capsids, plant leaves in buds, and geological folds are examples in nature of tightly packed low-dimensional objects. However, the general equations describing their deformations and stresses are challenging. We report experimental and theoretical results of a model configuration of compression of a confined elastic sheet, which can be conceptualized as a 1D line inside a 2D rectangular box. In this configuration, the two opposite ends of a planar sheet are pushed closer, while being confined in the orthogonal direction by two walls separated by a given gap. Similar compaction of sheets has been previously studied, and was shown to buckle into quasi-periodic motifs. In our experiments, we observed a new phenomenon, namely the spontaneous instability of the sheet, leading to localization into a single Yin-Yang pattern. The linearized Euler Elastica theory of elastic rods, together with global energy considerations, allow us to predict the symmetry-breaking of the sheet in terms of the number of motifs, compression distance, and tangential force. Surprisingly, the appearance of the Yin-Yang pattern does not require friction, although it influences the threshold of the instability.

Packing problems in confined geometries have attracted significant attention due to their relevance in science, engineering and technology. There is an attempt to optimize the available space while maintaining the stability and integrity of the packed objects. A useful classification of packing problems is via the dimensionalities of the packed objects d and of the confining container D. A classical case is when $D = d$, such as in sphere packing or granular matter [1, 2]. Not of less interest are lower dimensional objects, which can strongly deform due to high rotations, leading to non-linear geometrical deformations. 1D fibers [3] or 1D rods in 2D or 3D containers [4–8] are ubiquitous in nature, such as DNA in viral capsids [9, 10] or spider-capture silk inside droplets [11]. Similarly, a 2D plate in a 3D container [12] exhibits interesting phases, which are relevant in plant leaves in buds [13, 14] or geological folds [15]. However, the general equations describing deformations and stresses of tightly packed sheets or rods are challenging to solve [16–18].

In this Letter, we study a model system consisting of a compressed elastic sheet, which can be conceived as a 1D line inside a 2D rectangular box. The two opposite ends of a sheet are moved closer, while confined in the orthogonal direction by two walls separated by a given gap. A similar compaction was studied by Roman and Pocheau [19], but the gap between the two walls was decreased, while keeping the lateral length fixed. One can wonder whether the reported quasi-periodic buckled motifs [19–21] remain when the direction of compression is modified [22–31] and if this influences the stability diagram of the sheet. Surprisingly, we observe a spontaneous instability of the sheet, leading to the formation of a single Yin-Yang pattern, not reported before. Interestingly, this pattern is common to other confined configurations [32–36]. We measure experimentally both mechanical and geometrical properties of the sheet, during the lateral compression process. We also develop a theoretical description based on the Euler Elastica theory of elastic rods, and inspired by the work of Chai [25]. We demonstrate that the linearized theory describes well some regimes and properties and we identify the mechanisms necessary for the emergence of the spiraling instability. The appearance of the Yin-Yang pattern does not require friction, although the latter influences the threshold of the instability.

The experiment [Fig. 1(a)] consists of the

* stephanie.deboeuf@cnrs.fr

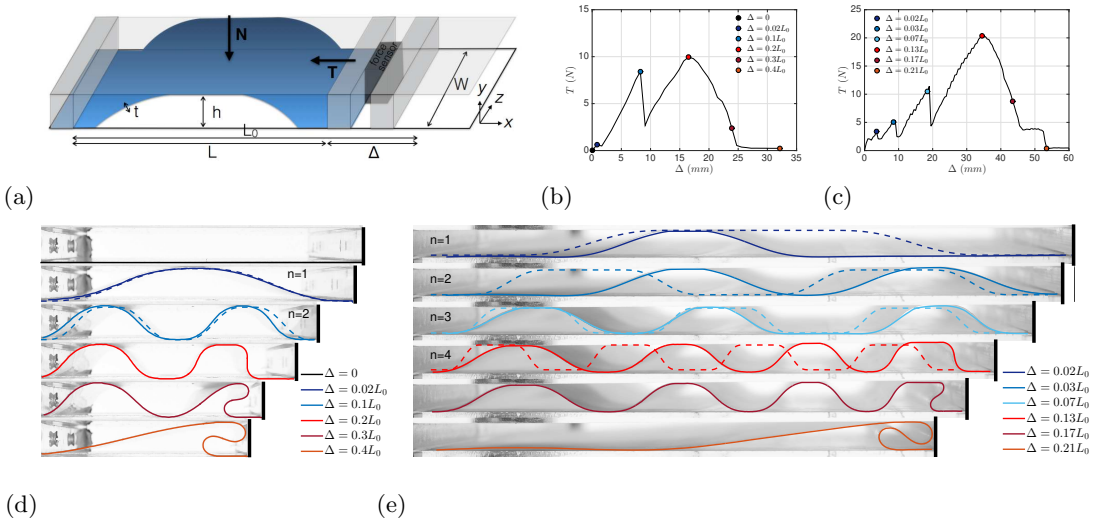

FIG. 1. (a) Scheme of the experiment of buckling of a planar sheet under bilateral constraints: the length, width and thickness of the sheet are L_0, W and t; the confining box is of height h and length $L = L_0 - \Delta$. A force sensor measures the tangential force T. (b)-(c) Tangential force T as a function of the compression Δ for two sets of experimental parameters: $h = 10$mm, $W = 20$cm; (b) $L_0 = 10$cm, $t = 100\mu$m, $E = 4$GPa; (c) $L_0 = 23.5$cm, $t = 120\mu$m, $E = 5$GPa. Colored circles correspond to pictures in (d)-(e), where sheet profiles at different compression distances Δ for the two configurations in (b)-(c) are shown. Between 1 and $n_{\max}$ motifs are observed, before the spiraling of the sheet (the Yin-Yang pattern) which is the final pattern observed in the experiments. The continuous and dashes lines are the experimental and theoretical predictions (using the linearized Elastica (2)), respectively.

compression of a planar sheet under bilateral confinement inside a limited box of height $h \sim 1$cm and lateral length $L = L_0 - \Delta \sim 10$cm, where Δ measures that compression ($h/L \sim 0.1$). Polyester (polyethylene terephtalate) sheets are characterized by a Young modulus $E \sim 1$GPa, length $L_0 \sim 10$cm, width $W \sim 10$cm and thickness $t \sim 100\mu$m ($L_0/t \gg 1$, $h/t \gg 1$). The bending modulus is determined by $B = Et^3/12(1-\nu^2) \in [10^{-5}, 10^{-2}]$J, where $\nu \simeq 0.4$ is the Poisson ratio. See the Supplemental Material for a table of the experimental parameters [37]. The morphology of the sheet is observed to be uniform along the z direction (namely along the width of the sheet), such that the experiment can be modeled as the compression of a 1D rod in a 2D rectangle. In essence, the lack of curvature along the z direction allows pure bending strains without stretching. Initially, the sheet is lying along the bottom wall, namely along $y = 0$. The sheet ends are clamped during the whole experiment.

During one realization, the gap height h is kept constant, while the compression distance Δ is slowly increased, at a velocity of around 0.5mm/s. From one realization to another, the experimental control parameters t, W, L_0, E and h are varied and several realizations are repeated for the same control parameters to investigate both the experimental reproducibility and the system multistability. A force sensor (Sensel Measurement, Futek LSB200 model) measures the tangential (compressive or tensile) force T exerted along the x direction, to which both elasticity and friction contribute. We denote the normal force exerted along the y direction by N. Simultaneously, pictures of the sheet profile are taken (NIKON D80 camera with 105mm objective).

As soon as we impose $\Delta \neq 0$ (Fig. 1), compressive tangential forces $T > 0$ appear [Figs. 1(b) and (c)] and the sheet buckles [Figs. 1(d) and (e)]. As a result, the sheet comes into contact with the top wall, lead-

ing to a response different from free buckling (without constraint) [38]. With further compression, the contacts with the walls extend, changing from point to line contacts. This leads to a hierarchical process, where the line contacts behave like shorter rod segments, which in turn buckle, and so on [Figs. 1(d) and (e)]. After the first buckling event, one motif is observed, made of two anti-symmetric free segments (a free segment being limited by contacts at both ends) and three contacts. Later, more motifs are formed when the longest line contact buckles, such that after n buckling events, the sheet exhibits n motifs, made of $2n$ free segments and $2n+1$ contacts. The pattern of line contacts and free segments is roughly periodic with more or less identical line contacts, free segments and motifs, due to metastability and friction forces. At each bucking event, when n changes to $n+1$ motifs, the tangential force T suddenly drops to a smaller value exhibiting a snap-through instability. In between buckling events, T increases continuously while increasing the compression distance Δ [Figs. 1(b) and (c)].

Instead of an ever-repeating sequence, as usually observed [19–31], these buckling events stop, when the sheet shows a strong symmetry-breaking. We observe that after $n_{\max}$ buckling events, the free segment located closest to the compressed end deforms strongly and non-linearly, by taking an S-shape [purple curves, Figs. 1(d) and (e)], that leads finally to the Yin-Yang pattern [orange curves, Figs. 1(d) and (e)]. Meanwhile, the tangential force T changes its behaviour - after reaching a maximum $T_{\max}$ at $\Delta_{\max}$, T continuously decreases to a small value [purple data points, Figs. 1(b) and (c)]. The final step is a last drop of T, corresponding to a last snap-through instability, which occurs when the S-shape spirals instantaneously, making all the other previous motifs disappear, and thus leaves the Yin-Yang pattern as the ultimate state [orange data points, Figs. 1(b) and (c)]. See the Supplemental Material for a video showing both the sheet profile and the tangential force during the compression [37].

We now wish to describe the sheet's profile and the evolution of the force during its compression. We can parameterize the sheet by the local slope $\theta(s)$ of the centerline of a cross-section normal to the z direction at each curvilinear position $s \in [0, L_0]$. See the Supplemental Material for a scheme indicating the notations [37]. This rod is modelled by the Euler Elastica equation, which can be written for each free segment as

$$BW\ddot{\theta}(s) = -T\sin\theta(s) + N\cos\theta(s), \qquad (1)$$

where T and N are the tangential and normal forces exerted on the rod along the x and y axes respectively. Considering $\theta(s) \ll 1$, Eq. (1) can be linearized, leading to

$$BWy''''(x) = -Ty''(x). \qquad (2)$$

The assumptions underlying Eq. (2) are satisfied for moderate compression distances ($\Delta \ll L_0$), but unjustified for large values of Δ, where any local slope θ reaches, and even exceeds, $\pi/2$. Note that describing the sheet using $y(x)$ in Eq. (2) cannot parameterize the S-shape or the Yin-Yang pattern where the local slope θ is not small, and hence $y(x)$ is no longer a function.

Additionally, the length conservation, for n identical free segments can be expressed as

$$\Delta \simeq n \int_0^H y'^2(x)dx, \qquad (3)$$

where $H = (L - \Sigma\,\ell)/2n$ is the projected length per free segment, with $\Sigma\,\ell$ being the total length of the line contacts.
Solving the differential Eq. (2) with its boundary conditions and imposing the length conservation (3), allows to obtain analytically the profile $y(x)$ and the force-compression relation $T(\Delta)$. Note that this analysis changes slightly for different situations: no contact, point contacts or line contacts.

When there is no contact, the tangential force T is proportional to the buckling force threshold T_{L_0}, times $(2\pi)^2$ for clamped boundary conditions, just like in free buckling [38], namely

$$T_{L_0} = \frac{BW}{L_0^2}. \qquad (4)$$

When the sheet is in contact with the walls ($n = 1$), the transition between point and line

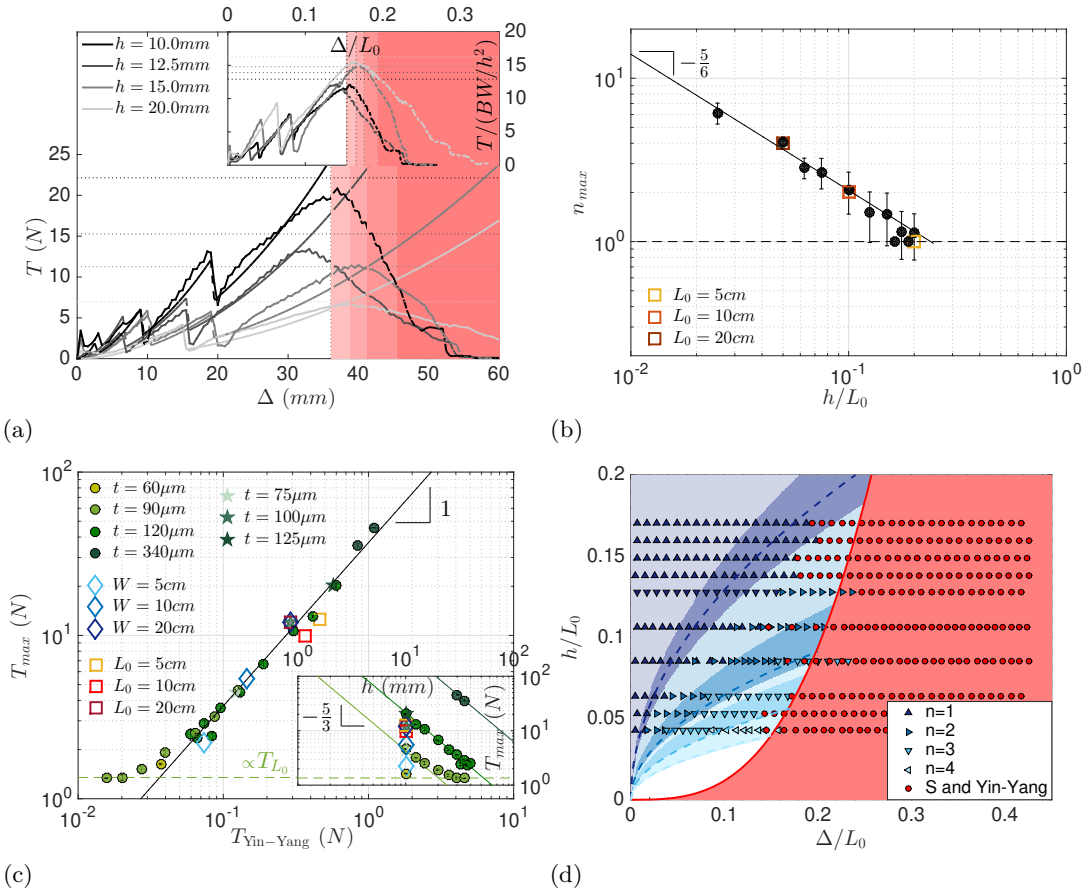

FIG. 2. (a) Tangential force T as a function of the compression distance Δ for a given elastic sheet ($W = 20$cm, $L_0 = 23.5$cm, $t = 120\mu$m, $E = 5$GPa) at different values of the gap h in the main panel, while dimensionless data $T/(BW/h^2)(\Delta/L_0)$ are plotted in the inset. The dashes curves are predictions from Eqs (6) and (7), while dotted lines are predictions of $\Delta_{\max}$ and $T_{\max}$ from Eqs. (13) and (14). (b) Maximal number of motifs $n_{\max}$ observed before the spiraling of the sheet as a function of h/L_0 and power law of exponent $-5/6$ [Eq. (12)]. The circles were averaged for different W, t, E and B at a constant $L_0 = 23.5$cm, while the squares correspond to different L_0. (c) Experimental measurements of the maximal compressive tangential force $T_{\max}$ ($\neq t, W, L_0$ and h indicated in legends) as a function of the prediction $T_{\mathrm{Yin-Yang}}$ [Eq. (14)], while the raw data $T_{\max}(h)$ are plotted in the inset. (d) Phase diagram that summarizes the possible configurations of the buckled elastic sheet (from 1 to 4 motifs and the S-shape/Yin-Yang state) in the plane of dimensionless bilateral constraints h/L_0 and Δ/L_0. The dashed and solid lines are predictions from Eq. (8) for several values of n (from 1 to 4) and Eq. (13) respectively. The shaded area around each dashed line represents an uncertainty region based on Eq. (7), which originates from the different possible patterns of line contacts.

contacts occurs when $TL_0^2 \simeq (4\pi)^2 BW$ (assuming contacts of identical lengths), so that already when Δ and T are moderate, the point contacts become line contacts. It turns out that point contacts do not appear anymore when $n \geq 2$: all the contacts are immediately lines after each buckling event [Fig. 1(e)] [25]. Since line contacts occur much more often, we will focus on this configuration in the following.

Assuming n identical motifs, the shape of a free segment is given by

$$y(x) = h\left[2\pi x/H - \sin\left(2\pi x/H\right)\right]/2\pi \qquad (5)$$

with $TH^2 = (2\pi)^2 BW$ and

$$T(\Delta) \simeq \frac{BW}{h^2}\left(\frac{4\pi\Delta}{3hn}\right)^2. \quad (6)$$

Note that the projected length of a single free segment, H, changes during the process. It decreases from $L_0/2n$, by $\Delta/2n$, due to compression, and by $\Sigma\,\ell/2n$, due to the elongation of line contacts.

The mode transition occurs when the line contact of maximal length ℓ buckles, when $T\ell^2 = (2\pi)^2 BW$. Therefore, different spatial patterns of line contacts may lead to different thresholds of mode transitions, even for the same total length $\Sigma\,\ell$. Hence, the mode transition thresholds $n(\Delta)$ cannot be uniquely predicted nor experimentally reproduced, because they are sensitive to the precise sequence of the buckling events. However, these thresholds are bounded by

$$n + 2n^2 \leq \frac{\Delta}{L_0}\frac{2}{3}\left(\frac{h}{L_0}\right)^{-2} \leq n + 4n^2. \quad (7)$$

The lower boundary corresponds to the case of a single line contact ($\ell = \Sigma\,\ell$), while the upper boundary corresponds to $(2n+1)$ contacts of identical lengths ($\ell = \Sigma\,\ell/(2n+1)$). An intermediate case is possible when each sequence of two line contacts separated by a free segment is duplicated $2n$ times, corresponding to a perfectly symmetric pattern ($\ell = \Sigma\,\ell/2n$), for which

$$\frac{\Delta}{L_0} = 6n^2\left(\frac{h}{L_0}\right)^2. \quad (8)$$

Thus, in the perfect symmetric and periodic case, one gets

$$n = \left\lfloor \sqrt{\frac{\Delta L_0}{6h^2}} \right\rfloor, \quad (9)$$

where $\lfloor . \rfloor$ is the floor function.

Concerning the morphology, the agreement of the linear approximation [Eqs. (5) and (9)] with experiments is quite good, as shown for two configurations in Fig. 1(d) and 1(e) for moderate values of Δ, especially when the motifs are fairly regular [Fig. 1(d)].

Concerning the force, the analytical expression (6) for $T(\Delta)$, with the number of motifs n that lies within the bounds given by Eq. (7), quantitatively describes the experiments (without adjustment), as can be seen in Fig. 2(a) for a given elastic sheet and different values of the gap h. Obviously, Eq. (6) does not capture the experimental measurement of $T(\Delta)$ for $\Delta \geq \Delta_{\max}$, where the sheet profiles are not properly captured by the linearized theory.

Combining Eqs. (6) and (9) highlights the characteristic force scale

$$T_h = \frac{BW}{h^2}, \quad (10)$$

that becomes relevant in bilaterally constrained systems, and which replaces T_{L_0} that is pertinent for free buckling. Indeed, the inset of Fig. 2(a) shows that rescaling T by T_h and Δ by L_0 allows to gather all curves.

Experimentally, the maximal number of motifs $n_{\max}$ before the appearance of the Yin-yang pattern decreases with h and increases with L_0 [Fig. 2(b)]. However, $n_{\max}$ is independent of all the other control parameters varied here (W, t, E). In order to understand $n_{\max}$, we compare the bending energy, measured by $BW\int_0^{L_0}\ddot{\theta}^2(s)ds/2$, of the configuration composed of n motifs of typical curvature $\ddot{\theta} \approx n^2 h/L_0^2$ (denoted by E_n) and the bending energy of a single Yin-Yang pattern of typical curvature $\ddot{\theta} \approx L_0/nh^2$ (denoted by $E_{\mathrm{Yin-Yang}}$). See the Supplemental Material for a scheme [37]. One finds

$$\frac{E_{\mathrm{Yin-Yang}}}{E_n} \propto \frac{1}{n^6}\left(\frac{L_0}{h}\right)^5. \quad (11)$$

We expect a transition between the two patterns (for $n = n_{\max}$) when the energy $E_{\mathrm{Yin-Yang}}$ falls below E_n, leading to the scaling law

$$n_{\max} \propto \left(\frac{h}{L_0}\right)^{-5/6}, \quad (12)$$

which is valid for small h/L_0 and $n_{\max} = 1$ valid for large h/L_0. This prediction is consistent with our experimental measurements, as shown in Fig. 2(b), with a prefactor 0.3. We

observe that $n_{\max}$ reaches 1 for $h/L_0 \geq 0.2$, this value appearing to be the characteristic aspect ratio between small and large h/L_0.

Being interested in the compression distance $\Delta_{\max}$ at which $n_{\max}$ is reached, we obtain from Eqs. (8) and (12) the scaling law

$$\frac{\Delta_{\max}}{L_0} \propto \left(\frac{h}{L_0}\right)^{1/3}, \tag{13}$$

valid for small h/L_0.

Based on these results [Eqs. (6), (12) and (13)], we obtain for the maximal force $T_{\max}$, which appears before the Yin-Yang transition, $T_{\max} \propto T_{\mathrm{Yin-Yang}}$ for small h/L_0, where

$$T_{\mathrm{Yin-Yang}} = \frac{BW}{L_0^{1/3} h^{5/3}} \tag{14}$$

is the characteristic force scale of the Yin-yang pattern. However, $T_{\max} \propto T_{L_0}$ for large values of h/L_0. This scaling law is compared, in the main panel of Fig. 2(c), with our experimental measurements, corresponding to different values of t, W, L_0 and h: the agreement is excellent, with a multiplicative constant 37; while raw data sets $T_{\max}(h)$ are shown in the inset. Note that $T_{\max}$ saturates at large values of h/L_0.

Fig. 2(d) shows the phase diagram of a confined elastic sheet, as a function of the lateral constraint h/L_0 and the compression constraint Δ/L_0. The states with $n = 1,\ 2,\ 3,\ 4$ motifs and the S-shape/Yin-Yang states are plotted as triangles and circles respectively. Several realizations with the same control parameters are presented in order to show the multistability of this system and the experimental reproducibility. This phase diagram does not depend on the properties of the elastic sheet, except for L_0. The dashed lines are predictions [Eq. (8)] based on the linearized Euler Elastica, assuming perfectly periodic segments. The shaded area around each dashed line represents an uncertainty region [Eq. (7)], which originates from the different possible patterns of line contacts. The solid line represents the predicted threshold for the non-linear deformation of the sheet [Eq. (13)], with the prefactor 0.44, determined from the previous experimental constants. All these mode transitions experimentally reported are well described by our predictions.

In this Letter, we studied the response of a thin sheet compressed from the side in a restricted volume. In particular, we provide a full phase diagram of the equilibrium state of a 1D line in a 2D container. We show that a pure elastic linear analysis provides a good qualitative and even quantitative description of the various mode transitions that the system exhibits. However, it fails to capture the transition to the Yin-Yang regime. Instead, a global energy consideration allows to determine this transition. We demonstrate the relevance of three force scales in bilaterally constrained buckling of an elastic sheet, namely: T_{L_0} for free buckling, T_h for buckling in a confined box, and most interestingly $T_{\mathrm{Yin-Yang}}$ for the transition towards the single Yin-Yang pattern.

The phase diagram we report applies to any 1D elastic sheet restricted to a 2D container, including the results reported in Roman et al. [19–21], where the container was compressed from above. The phenomenology of that system was apparently different, namely the modes were symmetric and most importantly the Yin-Yang regime was not observed. Our new phase diagram can explain this difference. First, typical initial conditions and the compression protocol used in [19] avoid altogether the Yin-Yang regime. Second, the presence of friction tends to enhance the symmetry breaking between the buckled segments, when the sheet is compressed from the side.

It would be interesting to extend our analysis to a full non-linear theory, particularly in order to describe the evolution at the Yin-Yang transition. Another important challenge is to consider the role of friction [7, 24, 39–41]. In particular, friction can block the sheet in places where the normal force exceeds a certain threshold, thus creating a smaller subsystem that continues to be compressed while screening the compressive forces from the rest of the sheet. A solid description of this system may lead to a better understanding of systems that are composed of multiple layers [42–45] and energy harvesting in bi-stable or multistable composites [29].

ACKNOWLEDGMENTS

We thank the students Célie Borilla, Vincent Buyle, Sophie Klintzing, Antoine Malod, Alexandre Richard, François Wu and Nassim Zeroual; Thierry Bastien and Laurent Quartier for their technical help; Anaïs Abramian, Florence Bertails-Descoubes, Olivier Devauchelle, Eric Lajeunesse and Sébastien Neukirch for scientific discussions.

[1] O. Pouliquen, M. Belzons, and M. Nicolas, Fluctuating particle motion during shear induced granular compaction, Phys. Rev. Lett. **91**, 014301 (2003).

[2] D. Cantor, M. Cárdenas-Barrantes, I. Preechawuttipong, M. Renouf, and E. Azéma, Compaction model for highly deformable particle assemblies, Phys. Rev. Lett. **124**, 208003 (2020).

[3] Y. Bhosale, N. Weiner, A. Butler, S. H. Kim, M. Gazzola, and H. King, Micromechanical origin of plasticity and hysteresis in nest-like packings, Phys. Rev. Lett. **128**, 198003 (2022).

[4] L. Boué and E. Katzav, Folding of flexible rods confined in 2d space, Europhys. Lett. **80**, 54002 (2007).

[5] J. Xiao and X. Chen, Buckling morphology of an elastic beam between two parallel lateral constraints: implication for a snake crawling between walls, J. R. Soc., Interface **10**, 20130399 (2013).

[6] M. Bayraktar and J. Männer, Cardiac looping may be driven by compressive loads resulting from unequal growth of the heart and pericardial cavity. observations on a physical simulation model, Front. Physiol. **5**, 112 (2014).

[7] J. Miller, T. Su, J. Pabon, N. Wicks, K. Bertoldi, and P. M. Reis, Buckling of a thin elastic rod inside a horizontal cylindrical constraint, Extrem. Mech. Lett. **3**, 36 (2015).

[8] J.-P. Liu, X.-Y. Zhong, Z.-B. Cheng, X.-Q. Feng, and G.-X. Ren, Buckling of a slender rod confined in a circular tube: theory, simulation, and experiment, Int. J. Mech. Sci. **140**, 288 (2018).

[9] E. Katzav, M. Adda-Bedia, and A. Boudaoud, A statistical approach to close packing of elastic rods and to dna packaging in viral capsids, Proc. Natl. Acad. Sci. USA **103**, 18900 (2006).

[10] D. Grossman, E. Katzav, and E. Sharon, Packing of stiff rods on ellipsoids: Geometry, Phys. Rev. E **103**, 013001 (2021).

[11] H. Elettro, S. Neukirch, F. Vollrath, and A. Antkowiak, In-drop capillary spooling of spider capture thread inspires hybrid fibers with mixed solid–liquid mechanical properties, Proc. Natl. Acad. Sci. USA **113**, 6143 (2016).

[12] S. Deboeuf, E. Katzav, A. Boudaoud, D. Bonn, and M. Adda-Bedia, Comparative study of crumpling and folding of thin sheets, Phys. Rev. Lett. **110**, 104301 (2013).

[13] H. Kobayashi, B. Kresling, and J. F. Vincent, The geometry of unfolding tree leaves, Proc. R. Soc. B **265**, 147 (1998).

[14] E. Couturier, S. C. Du Pont, and S. Douady, The filling law: a general framework for leaf folding and its consequences on leaf shape diversity, J. Theoret. Biol. **289**, 47 (2011).

[15] J. Hall, Ii. on the vertical position and convolutions of certain strata, and their relation with granite, Trans. Roy. Soc. Edin. **7**, 79 (1815).

[16] L. D. Landau, E. M. Lifshitz, A. M. Kosevich, and L. P. Pitaevskii, *Theory of elasticity: volume 7* (Elsevier, 1986).

[17] B. Audoly and Y. Pomeau, *Elasticity and Geometry. From Hair Curls to the Nonlinear Response of Shells.* (Oxford university Press, Oxford, 2010).

[18] O. M. O'Reilly, *Modeling nonlinear problems in the mechanics of strings and rods* (Springer, 2017).

[19] B. Roman and A. Pocheau, Buckling cascade of thin plates: Forms, constraints and similarity, EPL (Europhys. Lett.) **46**, 602 (1999).

[20] B. Roman and A. Pocheau, Postbuckling of bilaterally constrained rectangular thin plates, J. Mech. Phys. Solids **50**, 2379 (2002).

[21] A. Pocheau and B. Roman, Uniqueness of solutions for constrained elastica, Physica D: Nonlinear Phenomena **192**, 161 (2004).

[22] H.-G. Paap and L. Kramer, Wavenumber restriction in systems with discontinuous nonlinearities and the buckling instability of plates, J. Phys. **48**, 1471 (1987).

[23] H. Iseki, R. Sowerby, N. Chandrasekaran, and P. Gatt, The elastic-plastic snapping-through of a curved metal strip compressed between two rigid plates:(the influence of the sup-

ported end condition on the snap-through), JSME Int. J., Solid Mech., Strength Mater. **32**, 101 (1989).
[24] X. Chateau and Q. Nguyen, Buckling of elastic structures in unilateral contact, Eur. J. Mech. A Solids **10**, 71 (1991).
[25] H. Chai, The post-buckling response of a bilaterally constrained column, J. Mech. Phys. Solids **46**, 1155 (1998).
[26] P. Holmes, G. Domokos, J. Schmitt, and I. Szeberényi, Constrained euler buckling: an interplay of computation and analysis, Comp. Meth. Appl. Mech. Eng. **170**, 175 (1999).
[27] W.-C. Ro, J.-S. Chen, and S.-Y. Hong, Vibration and stability of a constrained elastica with variable length, Int. J. Solids Struct. **47**, 2143 (2010).
[28] W. Borchani, N. Lajnef, and R. Burgueño, Energy method solution for the postbuckling response of an axially loaded bilaterally constrained beam, Mech. Res. Commun. **70**, 114 (2015).
[29] S. Liu and R. Burgueño, Controlled elastic postbuckling of bilaterally constrained nonprismatic columns: application to enhanced quasi-static energy harvesters, Smart Mater. Struct. **25**, 125010 (2016).
[30] P. Jiao, W. Borchani, and N. Lajnef, Large deformation solutions to post-buckled beams confined by movable and flexible constraints: A static and dynamic analysis, Int. J. Solids Struct. **128**, 85 (2017).
[31] A. Liakou and E. Detournay, Constrained buckling of variable length elastica: Solution by geometrical segmentation, Int. J. Nonlinear Mech. **99**, 204 (2018).
[32] G. Domokos, W. Fraser, and I. Szeberényi, Symmetry-breaking bifurcations of the uplifted elastic strip, Phys. D **185**, 67 (2003).
[33] L. Boué, M. Adda-Bedia, A. Boudaoud, D. Cassani, Y. Couder, A. Eddi, and M. Trejo, Spiral patterns in the packing of flexible structures, Phys. Rev. Lett. **97**, 166104 (2006).
[34] S. Deboeuf, M. Adda-Bedia, and A. Boudaoud, Energy distributions and effective temperatures in the packing of elastic sheets, Europhys. Lett. **85**, 24002 (2009).
[35] J.-S. Chen and Y.-C. Lin, Vibration and stability of a long heavy elastica on rigid foundation, Int. J. Non-Lin. Mech. **50**, 11 (2013).
[36] X. Cheng, S. Xu, T. Jin, Z. Shen, and Y. Zhang, Bifurcation and mode transition of buckled ribbons under oblique compressions, Mech. Res. Comm. **131**, 104145 (2023).
[37] See Supplemental Material at [URL will be inserted by publisher] for a table of parameters used for the experiments, a video showing both the sheet profile and the tangential force during the compression and two schemes indicating the notations used for the calculations and the typical curvature for two configurations.
[38] L. Euler, *Methodus inveniendi lineas curvas maximi minimive proprietate gaudentes sive solutio problematis isoperimetrici latissimo sensu accepti (Zürich, 1744)*, Vol. 1 (Springer Science & Business Media, 1952).
[39] R. Vetter, F. K. Wittel, and H. J. Herrmann, Morphogenesis of filaments growing in flexible confinements, Nat. Commun. **5**, 4437 (2014).
[40] V. Romero, M. Ly, A. H. Rasheed, R. Charrondière, A. Lazarus, S. Neukirch, and F. Bertails-Descoubes, Physical validation of simulators in computer graphics: A new framework dedicated to slender elastic structures and frictional contact, ACM Trans. Graph. **40**, 1 (2021).
[41] S. Alben, Packing of elastic rings with friction, Proc. R. Soc. A **478**, 20210742 (2022).
[42] G. W. Hunt, Reflections and symmetries in space and time, IMA J. Appl. Math. **76**, 2 (2011).
[43] H. Badr, X. Zhao, S. Koumlis, G. Tucker, L. Lamberson, and M. Barsoum, Confined buckling in thin sheets and its correlation to ripplocations: A deformation mechanism in layered solids, Phys. Rev. Mater. **5**, 093603 (2021).
[44] H. Chai and D. Moshkovitz, On the post-buckling behavior of laterally constrained multilayers, Int. J. Solids Struct. **257**, 111827 (2022).
[45] A. Guerra, A. C. Slim, D. P. Holmes, and O. Kodio, Self-ordering of buckling, bending, and bumping beams, Phys. Rev. Lett. **130**, 148201 (2023).